







Spatial Distribution and Thermal Diversity of Surface Volatile Cold Traps at the Lunar Poles

Margaret E. Landis¹ , Paul O. Hayne^{1,2} , Jean-Pierre Williams³ , Benjamin T. Greenhagen⁴ , and David A. Paige³

¹Laboratory for Atmospheric and Space Physics, 3665 Discovery Drive, University of Colorado, Boulder, Boulder, CO 80303, USA

margaret.landis@lasp.colorado.edu

²Department of Astrophysical and Planetary Sciences, University of Colorado, Boulder, Boulder, CO 80309, USA

³Department of Earth, Planetary and Space Sciences, University of California, Los Angeles, Los Angeles, CA 90095, USA

⁴Johns Hopkins University Applied Physics Laboratory, Baltimore, MD 20723, USA

Received 2021 November 15; revised 2021 December 13; accepted 2021 December 15; published 2022 February 16

Abstract

The polar regions of the Moon host some of the most extreme low temperatures in the inner solar system due to its low obliquity, lack of atmosphere, and topographic relief. Some of these regions are already confirmed to host water ice. Proposed sources of water and other volatiles include lunar volcanic outgassing, solar wind, and comet impacts. Each of these possible sources would carry a potentially identifiable compositional signature beyond water. Determining the dominant sources of lunar volatiles, therefore, requires assessing the long-term thermal stability of an array of compounds. We present results of mapping the surface thermal stability locations of multiple key volatiles, including water, from the Diviner Lunar Radiometer data from 60° to 90° latitude in both hemispheres. We find the annual maximum temperature for each pixel of interest in the map (~300 m) to determine which volatiles of interest would be stable there. We report on the thermal stability area of each volatile, as well as the geologic context in some cases. We find that while the thermal stability area for volatiles is larger in the south pole generally, both the north pole and south pole host areas where potential tracer volatiles from lunar volcanism, solar wind, and cometary impacts would be thermally stable for billions of years if such volatiles were ever delivered. We find several areas equatorward of ~80° on the lunar nearside that could host water ice, where future missions could potentially access volatile deposits in order to place constraints on water delivery to the Moon.

Unified Astronomy Thesaurus concepts: [The Moon \(1692\)](#); [Planetary polar regions \(1251\)](#); [Surface ices \(2117\)](#)

1. Introduction

Lunar polar volatiles have been predicted and detected in the past through a series of methods, ranging from data-driven temperature models (e.g., Paige et al. 2010b) to direct detection via remote sensing or artificial impact experiment (e.g., Pieters et al. 2009; Colaprete et al. 2010; Hayne et al. 2010, 2015; Schultz et al. 2010; Li et al. 2018; Sefton-Nash et al. 2019). Neutron data suggest hydrogen enhancement at both poles (e.g., Feldman et al. 1998), consistent with the presence of water ice or hydrated minerals in the upper ~1 m of the surface. Buried water ice has been linked to changes in lunar crater depth-to-diameter ratios with latitude (Rubanenko et al. 2019), and increased hydrogen content could possibly be indicative of previous lunar polar orientations (Siegler et al. 2016). While the presence and role of water and potentially other ices in the lunar polar regions have been extensively documented, several key questions remain unanswered.

One open question is which mechanism has supplied hydrogen-bearing volatiles to the lunar polar regions. The three possible mechanisms are solar wind bombardment (e.g., Morgan & Shemansky 1991; McCord et al. 2011, and references therein), lunar volcanic activity (e.g., Needham & Kring 2017), and cometary impact (e.g., Gibson & Moore 1973). Lunar volcanic activity and cometary impact would result in trace volatiles plus water being delivered to the lunar poles. For example, lunar

volcanic activity is expected to result in more sulfur within a volatile deposit than water (Needham & Kring 2017), whereas a cometary-sourced deposit in sufficiently cold conditions would contain more water than sulfur, plus additional organic compounds (e.g., Bockelée-Morvan 2011). Surface polar volatile deposits could therefore contain a record of the delivery mechanisms and their relative contributions over time, which would then depend on age of the surface ice, preservation/destruction mechanisms, and the location of a datable horizon. Identification of regions that may record a nearly complete record of volatile delivery is key to determining where in situ observations would be critical. Identifying regions where temperatures are cold enough to prevent significant sublimation highlights regions where thermal loss can be largely eliminated as a possible removal mechanism. This allows for the simplification of mass balance models for understanding in situ observations.

Understanding the ultimate sources and rates of lunar volatiles is also key to understanding their potential use as a resource during future human activity on the lunar surface. The Moon's south pole is a proposed site for future exploration by both robotic and human missions, as described in NASA's plans for the next decade of lunar exploration (e.g., Clarke 2019), and including the upcoming Volatiles Investigating Polar Exploration Rover (VIPER), Polar Resources Ice Mining Experiment (PRIME-1), and Commercial Lunar Payload Services (CLPS) 19-C (Masten-1). By understanding where water ice and other volatiles could be stable at the surface, future missions could be directed to locations where water and the most or least additional potential volatiles depending on science goals. Some volatiles that are found in comets, like hydrogen cyanide and toluene (e.g., Bockelée-Morvan 2011), can



Original content from this work may be used under the terms of the [Creative Commons Attribution 4.0 licence](#). Any further distribution of this work must maintain attribution to the author(s) and the title of the work, journal citation and DOI.

Table 1
Volatiles of Interest in This Study and Resulting Predicted Thermal Stability Area

Chemical Formula	Name	M (g mol ⁻¹)	T_v (K)	% Relative to H ₂ O		North		South	
				Comets	Lunar Mare Degassing	60°–90° (km ²)	>80° (km ²)	60°–90° (km ²)	>80° (km ²)
N ₂	Nitrogen	28.02	16.2	≤0.09	≤0.09	≤0.09	≤0.09
CO	Carbon monoxide	28.01	18.2	23	4444–8333	≤0.09	≤0.09	≤0.09	≤0.09
Ar	Argon	39.95	19.5	≤0.09	≤0.09	≤0.09	≤0.09
Kr	Krypton	83.8	24.5	≤0.09	≤0.09	≤0.09	≤0.09
Xe	Xenon	131.3	36.1	≤0.09	≤0.09	≤0.09	≤0.09
H ₂ S	Hydrogen sulfide	34.09	50.6	1.5	...	≤0.09	≤0.09	5	5
CO ₂	Carbon dioxide	44.01	54.3	12	...	0.18	0.18	20	20
NH ₃	Ammonia	17.03	65.5	1.5	...	99	99	554	554
NH ₄ SH	Ammonium hydrosulfide	51.12	96.1	3102	3074	7887	7716
SO ₂	Sulfur dioxide	64.07	62.3	0.2	...	38	38	273	273
H ₂ O	Water	18.02	106.6	100	100	5513	5414	11,888	11,434
S	Sulfur	32.07	201.5	...	6000–10,000	48,782	35,811	64,837	44,828
CH ₄	Methane	16.04	22	1.5	...	≤0.09	≤0.09	≤0.09	0
OCS	Carbonyl sulfide	60.08	46.8	0.4	...	≤0.09	≤0.09	0.9	0.9
C ₅ H ₁₂	Pentane	72.15	73.6	472	472	1818	1810
CS ₂	Carbon disulfide	76.15	74.4	0.3	...	516	516	1991	1982
HCN	Hydrogen cyanide	27.03	80.5	0.25	...	896	894	3328	3305
C ₇ H ₅	Toluene	92.13	87.6	1589	1579	5134	5070
C ₅ H ₁₀ O	3-Pentanone	96.21	92.8	2432	2412	6753	6634
NH ₄ CN	Ammonium cyanide	44.06	93.8	2629	2607	7104	6971
C ₅ H ₁₀ O ₂	Ethyl propionate	102.13	103.6	4804	4733	10,629	10,279
NH ₄ CO ₂ NH ₂	Ammonium carbonate	78.08	107.4	5700	5591	12,238	11,751
NH ₄ HCO ₃	Ammonium bicarbonate	79.06	113.3	7008	6811	14,818	13,986

Note. For the volatiles of interest in this study, the volatility temperature (e.g., temperature at which ≤ 1 mm Gyr⁻¹ of Sublimation will occur, T_v), and the areas at both North and South Poles from 60° to 90° and >80° latitude are given in this table. We include the abundance of volatiles where applicable relative to water from comets (Bockelée-Morvan 2011) and lunar outgassing (Needham & Kring 2017). Molecular mass (M) and stability temperatures (T_v) are from Zhang & Paige (2009). Areas less than 1 Diviner pixel are given as ≤ 0.09 km². Some volatile areas are not plotted in the volatile maps due to the minimum requirement in the map that at least 2 pixels be touching to be counted in the overall mapping. Diviner lunar bolometric temperatures from which temperatures can be converted to areas are given in the supplemental information.

be potentially toxic to humans. Finally, understanding the delivery rate of water to the Moon can inform in situ water resource management, including understanding how these deposits are being replenished, if at all. Thermal stability maps are also useful guides in terms of candidate species that may be detected through ongoing and future remote sensing and in situ efforts.

We present the potential locations of condensed surface volatiles based on bolometric temperatures derived from Lunar Reconnaissance Orbiter’s (LRO) Diviner Lunar Radiometer data (Paige et al. 2010a) from 60° to 90° latitude in both hemispheres based on thermal stability alone. A primary motivation for this study is to quantify and map the thermal stability regions for volatiles other than water. Also significant is the broader latitude range of our investigation than previous studies (e.g., Paige et al. 2010b; Williams et al. 2019) and the addition of several more years of data from previous global maximum temperature maps (Williams et al. 2017). This broader spatial and temporal coverage enables identification of potential regions of water ice stability that are more accessible to future missions, from a thermal

management and communication standpoint. Developing a more spatially expansive picture of the cold traps for a variety of volatiles in the northern and southern hemispheres allows for more complete comparisons between other regional data sets (e.g., Feldman et al. 1998), observations of geomorphological trends (e.g., Rubanenko et al. 2019), and previous predictions of permanently shadowed regions from topography (e.g., McGovern et al. 2013). Therefore, expanding the latitude range considered in this study offers the opportunity not only to complete the catalog of low-temperature areas in the polar regions but also to understand the potential diversity of volatiles within permanently shadowed regions (PSRs) due to thermal conditions. We can identify key differences between lunar poles in terms of an expanded search for surface volatile stability areas as well.

We use Diviner data for 10 yr from 2009 to 2019 in order to calculate maximum surface temperatures, and we consider a variety of potential surface volatiles that could be present in addition to water due to lunar volcanism and cometary impacts (Table 1). We compare the maximum surface temperature to

the 1 mm Gyr⁻¹ loss rate temperature from Zhang & Paige (2009) to determine regions of surface stability for that volatile of interest, an inherently conservative constraint on the long-term thermally predicted location of volatiles. We identify regions within PSRs that host multiple species of volatiles, including hydrocarbons and other volatiles that may be fingerprints of cometary and lunar volcanism contribution to the current water ice budget of the Moon. Some of these compounds may possibly present a human health risk if present in high enough quantity (e.g., hydrogen cyanide). We discuss implications for future in situ exploration, including possible target areas where sampling could help determine the long-term relative delivery rates from known volatile sources. Additionally, we quantify present-day hemispheric differences in surface water ice stability and discuss nearside, lower-latitude surface water ice areas that may be more accessible for future lunar missions. We quantify the predicted thermal stability regions for a broad range of volatiles in a wider latitude range than has been previously considered, and we describe those regions' potential role as sites of interest for future lunar exploration.

2. Data and Mapping

2.1. Data Retrieval and Processing

LRO's Diviner radiometer instrument has been collecting data at the Moon since 2009 July. Diviner measures radiances from the surface of the Moon over nine spectral channels, which can then be integrated to derive representative bolometric surface temperatures (Paige et al. 2010b). Roughness elements, such as sub-meter-scale slopes and shadowing, within the Diviner detector footprint can cause variations in radiance from small, subpixel areas that may be unresolved yet significantly contribute to the area where a volatile can be stable (e.g., at small scales on the Moon; Bandfield et al. 2015; Rubanenko & Aharonson 2017; Davidsson & Hosseini 2021; Hayne et al. 2021). Therefore, bolometric temperatures derived from Diviner measurements represent a weighted average of the true surface temperature distribution contained within pixels over ~250 m in scale (the approximate Diviner lunar radiometer footprint), which does not rule out colder areas within the ~250 m pixel or areas outside that may be singly or doubly shadowed and take up a small portion of a typical pixel. The specifications of the Diviner lunar radiometer are described in full in Paige et al. (2010a, 2010b), including details on the conversion of measured radiances to bolometric temperatures.

We use Diviner data from 2009 August to 2019 January (an interval of 10 Draconic years) poleward of 60° latitude in both hemispheres of the Moon. We spatially bin the data such that each bin in the map is equal to 0.01° in the polar azimuthal equidistant projection (Figure 1). Polar azimuthal equidistant projection is an area-preserving projection, so each 0.01° pixel is equal to ~0.09 km² (i.e., side length of ~300 m). To minimize photometric variations and emission phase function effects due to large spacecraft rolls and off-nadir targeted observations, we limit emission angles to less than 10°. We further remove data with event flags from non-nadir pointing nominal data mode. We also excluded data from 21 orbits (included in the supplemental information, access information in the acknowledgments, <<1% of all LRO orbits in 10 Draconic years, e.g., >40,000 orbits) that contained miscalibrations, with significantly warmer temperatures compared to

all other orbits (so-called “hot orbits”), and then removed all acquired during unique spacecraft and natural events such as lunar eclipses. The radiance data were separated into lunar day (6–18 hr local time) and lunar night (18–6 hr local time) and averaged over each degree of ecliptic longitude (L_s ; e.g., Schorghofer & Williams 2020) in order to maximize signal-to-noise ratio for low surface temperatures. The separation into day/night maps of lunar temperature is necessary because some terrains, especially high slope ones near the pole, can have their maximum surface temperatures occur between the hour angles of 18 and 6 (Williams et al. 2019, Figure 10). The binned radiances, in ~1 lunar day intervals separated by day/night, were used to calculate maximum temperatures.

The L_s -binned day/night radiances were then used to calculate bolometric temperatures for that surface pixel following the equations given in Paige et al. (2010b), where the flux is calculated using a weighted sum

$$\sigma T_{\text{bol}}^4 = \sum_{i=3}^9 \sigma T_i^4 f(T_i, \lambda_1, \lambda_2), \quad (1)$$

where T_{bol} is the bolometric temperature, i the channel number, T_i the brightness temperature, and f a weighted average based on the wavelengths of each Diviner channel. The equation for this weighting factor is given in Paige et al. (2010b). This bolometric temperature was calculated for each pixel for each 1 L_s degree for both daytime and nighttime bins included in the mapped data from the average radiance as described above. The resulting average radiance used as input is controlled for diurnal and seasonal effects by binning by day/night and L_s , such that the resulting radiance is the average radiance at that pixel on that day/night of the lunar year for 10 lunar years. This helps reduce the one-time effect of spurious high radiances especially in cold regions in longer-wavelength channels where the noise-equivalent temperature difference is large compared to the bolometric temperature.

This step results in an array of bolometric temperatures broken down by day/night and day of the lunar year (L_s) for 10 Draconic years of Diviner data. From there, the maximum temperature over the course of a lunar year (1–360 L_s) was determined by taking the maximum temperature from that pixel from all of the daily temperature maps. To determine the maximum, we use the following maximum finding rule:

$$T_{\text{annual max}} = \max_{\text{day/night}} [\max_{L_s} (T_{\text{bol}})]. \quad (2)$$

Our resulting maximum temperatures for both poles (Figure 1) are consistent with Williams et al. (2019). We note that data for bins close to the pole are affected by the drift in LRO's orbit away from a pole-crossing orbit, as previously described in Williams et al. (2019). This means that data in those locations do not exist for the entire time period of interest; however, there are still multiple Draconic years of data at these locations before the LRO orbit drifted to lower inclinations.

Recent work has suggested that maximum temperature may not fully characterize surface thermal stability of volatiles, as the duration for which the maximum temperature occurs is too short compared to more moderate temperatures over the course of the diurnal and annual cycles (Schorghofer & Williams 2020). Nonetheless, we continue to use the annual maximum temperature in this work, which provides the strongest upper limit on a given volatile's sublimation rate at

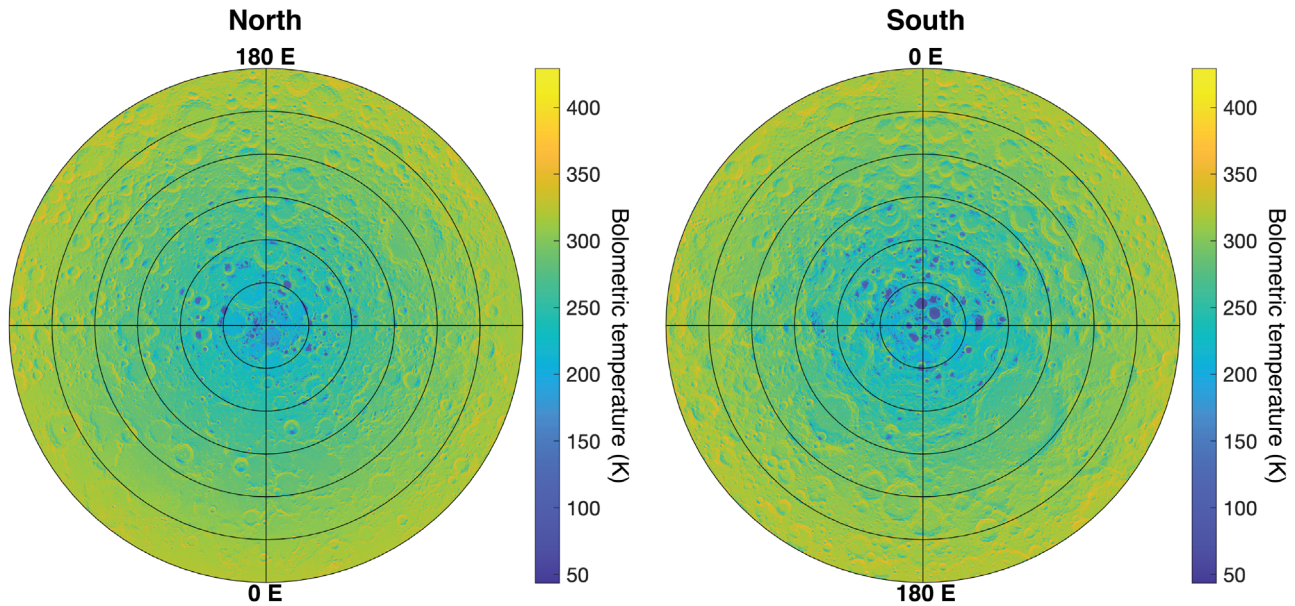


Figure 1. Maximum bolometric temperatures for the north (left) and south (right) poles derived in this study and used to determine surface thermal stability regions for volatiles, displayed in polar azimuthal equidistant projection. Each latitude ring is 5° .

a given location. Therefore, this provides a conservative estimate of volatile thermal stability areas and identifies locations most likely to host nearly permanent, long-term records of volatile transport to the Moon from a thermophysical perspective. A lack of a specific volatile species in a stable region in this case, for example, would indicate a low supply rate and/or rapid destruction/burial rate with a high degree of confidence versus a more spatially extensive thermal stability region where volatiles may temporarily have higher sublimation rates over some part of the lunar year.

2.2. Surface Volatile Thermal Stability Criteria

From the Diviner bolometric temperature maps, we define surface volatile thermal stability regions based on the volatility temperatures given in Zhang & Paige (2009) (Table 1). Regions where the Diviner maximum bolometric temperature is less than the volatility temperature define the surface thermal stability area for each volatile. The Zhang & Paige (2009) volatility temperatures correspond to a surface volatile loss rate of 1 mm Gyr^{-1} . Some variation in thermal stability area will occur depending on the volatile loss rate used as a stability criterion, and the 1 mm Gyr^{-1} rate was chosen in order to limit the areas detected to be some of the most likely to host the volatiles of interest, if their delivery rates to the Moon’s polar regions are sufficiently high.

We use a linear radiance mixing model to examine the effect of some fraction of the areal extent of a Diviner pixel being occupied by lower temperatures. For example, CO_2 has a stability temperature near the coldest annual maximum temperatures measured by Diviner at the south pole. From Table 1, CO_2 ice would sublimate at a rate of 1 mm Gyr^{-1} at $\sim 54 \text{ K}$. To provide a simple estimate of the unresolved cold trap area, we assume a linear mixing model for the radiances from a two-component source, such that the total radiance is equal to

$$R_\lambda = f_{\text{cold}} B_\lambda(T_{\text{cold}}) + (1 - f_{\text{cold}}) B_\lambda(T_{\text{hot}}), \quad (3)$$

where R_λ is the measured spectral radiance at wavelength λ , f_{cold} the area fraction of the Diviner pixel with some temperature less than the total pixel brightness temperature, and $B_\lambda(T)$ the spectral radiance of a blackbody at temperature T . The modeled final spectral radiances can then be numerically integrated to bolometric temperature following the procedure described in Paige et al. (2010a). This simple approach encompasses effects from small topographic surface elements considered in Hayne et al. (2021) and Davidsson & Hosseini (2021) with a broad consideration of how much sub-Diviner-pixel thermal variation would be indistinguishable in the resulting final bolometric temperature from a surface all at the calculated bolometric temperature. It is important to recognize that the bolometric temperature is an inferred temperature at a scale of hundreds of meters, and that small temperature variations over small scales are still important for understanding very localized thermal stability zones.

Using the above approach, we find that for a 60 K bolometric temperature, which would not be included in the Diviner-based map as a region of CO_2 ice surface thermal stability, up to $\sim 20\%$ of that pixel could be as much as 6 K colder than the pixel’s bolometric temperature assuming the same emissivity for the entire surface. The change in temperature varies when taking into account the noise-equivalent temperature differences (Paige et al. 2010a) for different Diviner channels, and depending on channel, the area could be between $\sim 30\%$ and 50% of the pixel. Therefore, a Diviner measurement of a 60 K bolometric temperature pixel does not rule out the presence of a significant fraction of that pixel being below the observed bolometric temperature due to subpixel temperature mixing, or emission or phase angle effects from Diviner. Additionally, if different surface elements have an emissivity less than 1, the variations in true temperature of the surface might be even higher. There is evidence at other locations, like Amundsen crater, for doubly and triply shadowed regions of PSRs significantly decreasing the surface temperatures within a Diviner observation footprint (Sefton-Nash et al. 2019). The

subpixel mixing effects of smaller roughness elements, e.g., meter and submeter slopes and shadows, on final bolometric temperature have also been demonstrated to be significant (Davidsson & Hosseini 2021; Hayne et al. 2021).

To understand the fraction of a pixel that could be colder than the scene bolometric temperature from surface roughness, we used the rough-surface thermal model from Hayne et al. (2021) to estimate the subpixel temperature distribution within the Diviner measurement footprint. First, we generated a surface using a random distribution of slopes with rms values of 6° and 27° . Then, we scaled the incident fluxes appropriately to reach a bolometric temperature of 60 K for this whole surface, representing one Diviner pixel. The fraction of the subpixel surface elements below a specific temperature could then be calculated. For a cutoff of 54 K in the temperature distribution within the 60 K bolometric temperature pixel, we found that roughly 22% and 44% of the pixels were colder than this value, for rms slopes of 6° and 27° , respectively. The lower end of this range is consistent with the results of the simple two-component model above. Although the rms slopes within the PSRs are not well known at all relevant scales (e.g., Mazarico et al. 2011), the dominant scales in determining thermal stability should be roughly 10 cm, corresponding to rms slopes within the range reported here (Hayne et al. 2021). Therefore, from both the linear mixing model and the surface roughness model, we would expect $\sim 20\%$ or more additional area where volatiles would actually be thermally stable on the surface of the Moon within pixels where the bolometric maximum temperature is slightly above the cutoff for volatile thermal stability.

2.3. Map Generation

Maximum temperature maps are given in Figure 1 in polar azimuthal equidistant projection. We also mapped surface volatile thermal stability based on these temperatures, using the criteria described above. The surface thermal stability areas are reported for each volatile in Table 1, from 60° to 90° and from 80° to 90° latitude for both hemispheres. The Diviner maximum temperature data are also archived as a supplement to this paper, with the DOI given in the acknowledgments.

In order to generate shapefiles, which contain polygon features plottable by Geographic Information Systems (GIS) software (also archived as part of the supplemental information), we used the built-in *bwboundaries* image edge detection algorithm in MATLAB to identify contiguous regions of volatile thermal stability within 8 adjacent pixels. Therefore, the maps compatible with GIS software do not include small, 1 pixel areas of thermal stability that are otherwise included in the areas calculated in Table 1. Vertices of these areas were converted to latitude and longitude and saved as GIS compatible shapefiles using the MATLAB function *polyshape*. The Diviner maximum data preserve all thermal stability locations based on temperature, whereas the GIS visualization may miss small, 1 pixel areas of thermal stability but increases compatibility with other GIS software. The results of the volatile thermal stability map generation of GIS shapefiles are shown in Figures 2–5.

3. Results and Discussion

Our list of volatiles of interest in this study, their volatility temperatures, and areas of surface thermal stability poleward of

60° latitude in each hemisphere are given in Table 1. The areas given here are those where the temperature of the entire Diviner pixel is below the volatility temperature listed. For some volatile species, there are no pixels in the maximum temperature map meeting the $<1 \text{ mm Gyr}^{-1}$ sublimation rate criterion. We record these as being less than the area of one $\sim 300 \text{ m}$ Diviner temperature map pixel. However, multiple shadowing due to surface roughness could result in subpixel temperatures spanning a wider range than those measured by Diviner, potentially providing additional cold trap areas for these highly volatile species. Therefore, areas listed in Table 1 represent the thermal stability areas on the Diviner-pixel scale and do not account for unresolved cold traps.

Previous studies (e.g., Shearer et al. 2006; Zhang & Paige 2009; Needham & Kring 2017) have considered atomic sulfur, S_1 , in their consideration of the dominant sulfur species that would be likely derived from lunar volcanism. There exist many allotropes of sulfur (e.g., Meyer 1964; Steudel & Eckert 2003) that may also be present on the Moon that measurement would resolve. Here we follow previous authors and focus on S_1 . Depending on subsequent modification of any erupted sulfur species in a tenuous lunar exo- or atmosphere or on the surface, sulfur-specific chemistry may affect how much S is available to be directly ballistically transported from volcanic regions to the polar regions. Additionally, H_2S and SO_2 likely co-occurred and may be converted to S through photolysis instead of lost to space through sublimation at some as-yet-known rate. Here we focus on H_2S I. However, there are other phases of H_2S that could be present at the south pole that may be less volatile, though their presence and abundance remain an open question (e.g., Schorghofer et al. 2021). Sulfur may also be generated by impact vaporization or sputtering from FeS (Killen 2003) and lost to space or resupply of S to the polar regions depending on local troilite abundance. Therefore, one caution with this work is that if elemental S is not observed in all thermally stable locations, it could also be due to the original nature of lunar volcanism, and lack of S presents an upper limit on the total final value of that volatile delivered by lunar outgassing and through the transient atmosphere. The S/ H_2O ratio therefore is a critical parameter to be measured rather than S abundance alone by future missions, as well as the relative abundances of S-bearing species to each other and nearby troilite deposits.

The detailed, highly accurate maps of polar surface temperatures presented here have a range of applications for understanding lunar polar volatiles. In particular, we first identify regions with temperatures conducive to cold-trapping for a range of volatile species that could be measured using remote sensing or in situ techniques to identify volatile sources on the Moon. Several of these cold traps are located within well-known PSRs. Second, we use the thermal stability maps to identify off-polar (latitude $< 80^\circ$) nearside cold traps for water ice that have not been previously recognized, which may prove to be more accessible to future surface missions. Third, we note the prominent hemispheric dichotomy in polar shadowing and temperatures on the Moon and discuss its implications for volatile thermal stability. Finally, we summarize implications for future exploration, both robotic and human, in the context of the maps of potential thermal surface stability regions for key volatiles.

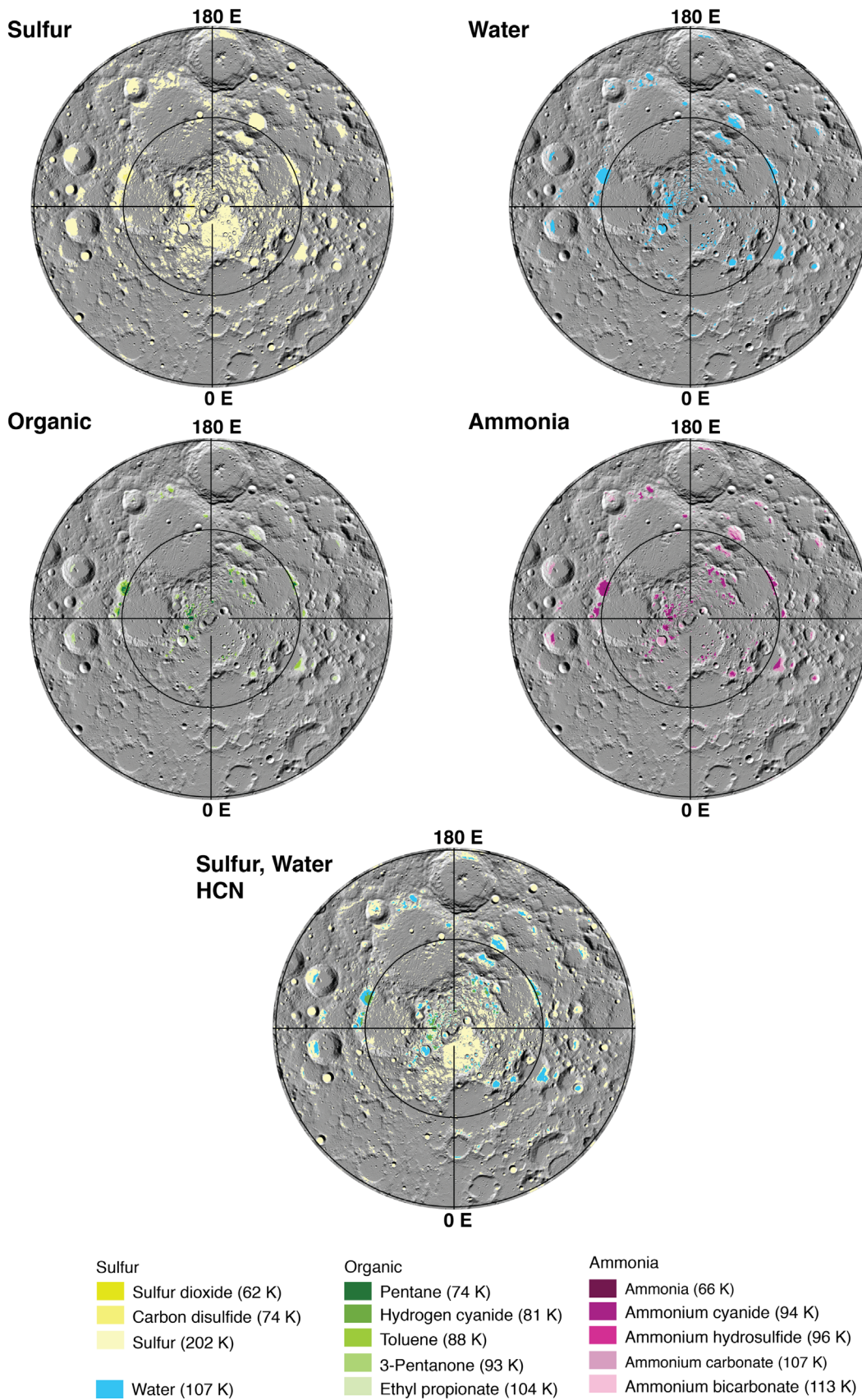


Figure 2. Polar stereographic display of the volatile species of interest that have surface thermal stability regions at the north pole from 80° to 90° N (species and stability temperature given in the legend). Background data are the Lunar Orbiter Laser Altimeter (LOLA) 100 m pixel⁻¹ shaded relief map. Each ring is 5° latitude.

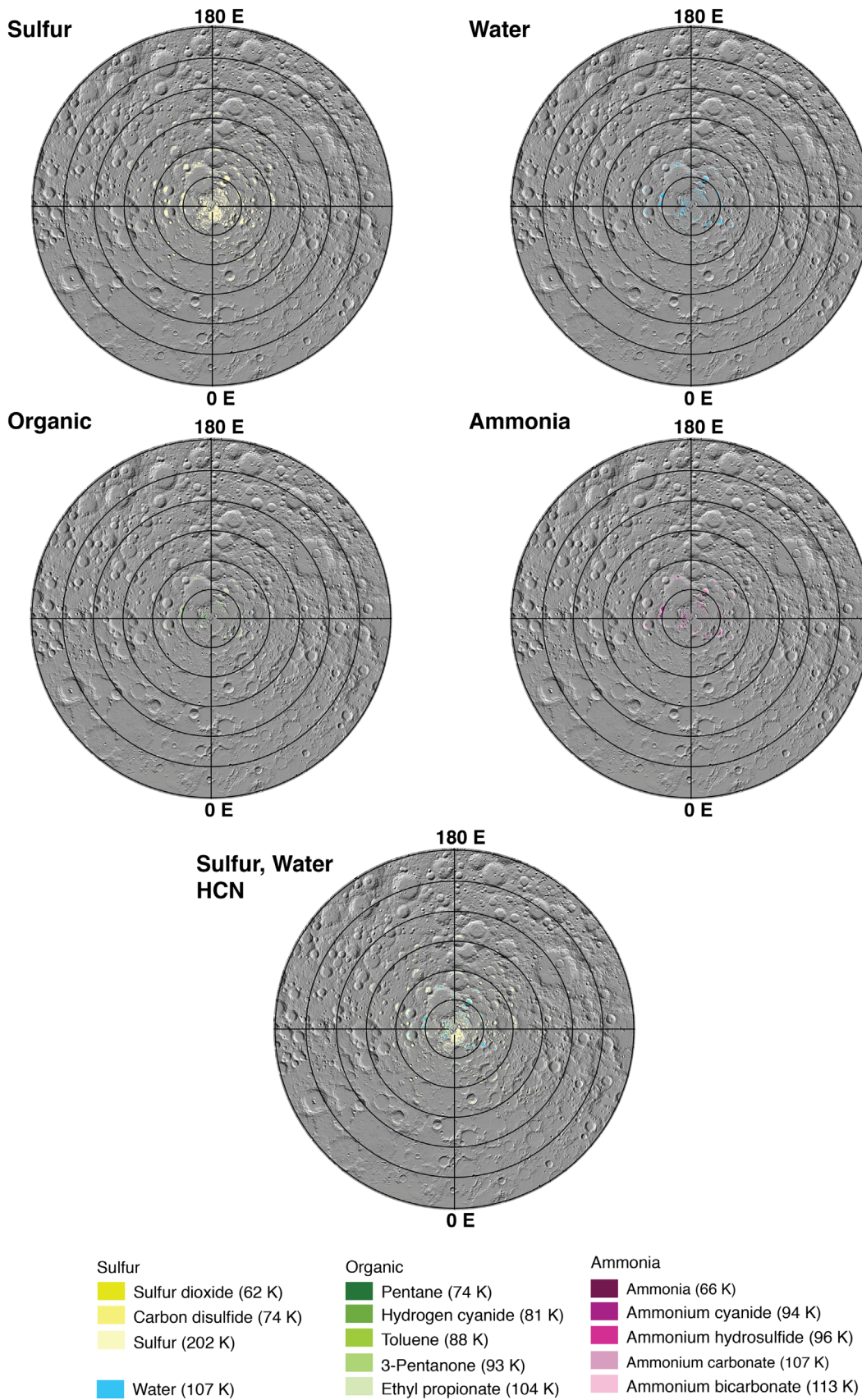


Figure 3. Polar stereographic display of the volatile species of interest that have surface thermal stability regions at the north pole from 60° to 90° N (species and stability temperature given in the legend). Background data are the Lunar Orbiter Laser Altimeter (LOLA) 100 m pixel⁻¹ shaded relief map. Each ring is 5° latitude.

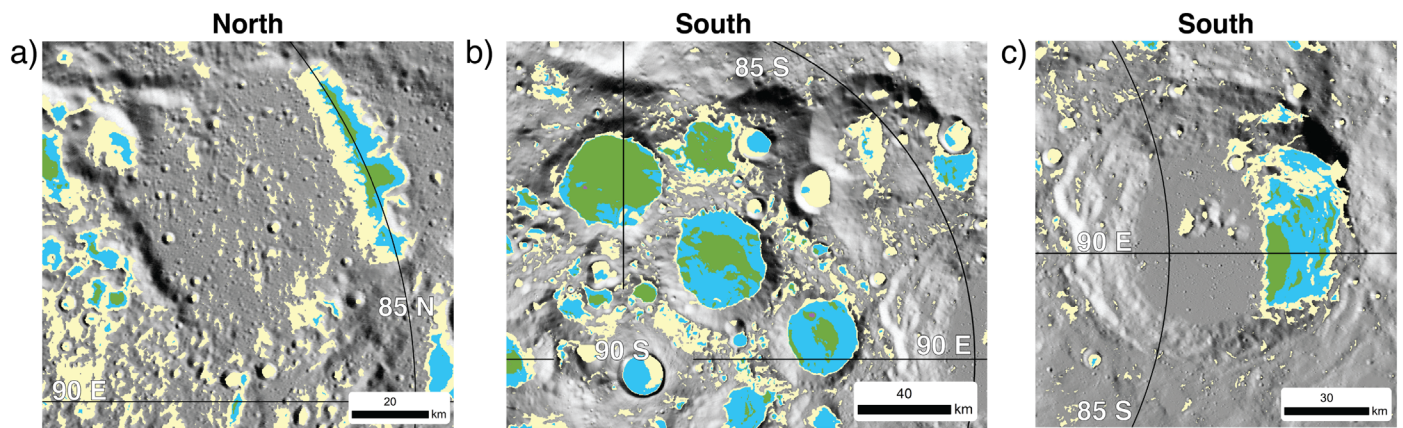


Figure 6. The locations of sulfur (yellow), water (blue), hydrogen cyanide (green), and CO_2 (purple) in the same color scheme as the regional maps previously shown, at (a) Rozhdestvenskiy W crater at the north pole; (b) Haworth, Shoemaker, and Faustini craters at the south pole; and (c) Amundsen crater at the south pole. While the PSRs at Haworth, Shoemaker, and Faustini are more poleward and in smaller craters than Amundsen and Rozhdestvenskiy W craters, this region spans the final study sites for the VIPER rover landing site and includes Nobile crater, the landing site selected at the time of writing. Major latitude and longitude lines within the figure are labeled.

3.1. Areas with the Most Diversity of Volatiles and Accessibility

We identify several locations where in situ compositional characterization of surface materials would help quantify the dominant present-day sources of lunar volatiles. These are locations where possible volcanic (e.g., sulfur) and cometary (e.g., hydrogen cyanide and other complex organics) volatiles could co-occur with water. In situ detection of these species and their abundances relative to water would place constraints on the long-term volatile supply and source to the Moon. Map layers in the figures are from lowest volatility temperature on top to highest on bottom, so the coldest locations contain the volatile of interest, as well as all less volatile species (Figures 2–5). Several of these locations, such as the floor of Amundsen crater ($\sim 81^\circ \text{S}$, 83°E , Figure 6), are associated with low slopes and persistently or permanently shadowed regions relatively close to sunlit terrain, providing enhanced accessibility for spacecraft landing on or traversing that region (e.g., Lemelin et al. 2014, 2021). These locations could offer favorable locations for sampling and characterizing any extant volatile deposits to unlock the Moon’s volatile history. A region near Nobile crater (the landing site for the VIPER rover at time of writing) is included in the sites with thermal stability of a diverse range of volatile species, though other sites with diverse surface thermal stability regions occur at both poles and also at slightly more equatorward latitudes. Three of the regions where there are thermal stability areas for multiple volatiles are described in the following subsections.

3.1.1. North Pole: Rozhdestvenskiy W ($\sim 86^\circ \text{N}$, 116°E)

At the north pole, a notable offset is present in the largest surface volatile thermal stability regions relative to the pole due to more pronounced variations in topography near $\sim 85^\circ \text{N}$. This is in contrast to the south polar region, where, due to happenstance of the locations of well-preserved, deep craters, volatile thermal stability increases monotonically toward the pole (see Section 3.3). One region of interest where sulfur (S), water, and hydrogen cyanide would all be predicted to be stable is at Rozhdestvenskiy W, a ~ 75 km diameter crater centered near 86°N , 116°E (Figure 6(a)). The southern (pole-facing) wall of the crater casts a shadow onto the crater floor, and the scalloped southern rim causes sufficient shadowing for

hydrogen cyanide (sublimates $< 1 \text{ mm Gyr}^{-1}$ at $\sim 81 \text{ K}$) to be stable in some portions of the crater wall and floor.

This crater is also notable for its flat floor pockmarked by smaller craters. A traverse path could sample multiple scales of shadowing and volatile thermal stability along the floor here while avoiding unplanned drives into small craters. In situ measurements could examine both ancient preservation of volatiles through Diviner-scale, large thermal stability regions and current processes through the smaller, rough areas in the illuminated crater floor. One disadvantage to this site is that it is located on the lunar farside, complicating communication to Earth.

3.1.2. South Pole: Haworth, Shoemaker, and Faustini Craters and Amundsen Crater

The lunar south pole is notable for the number of broad-PSR-containing craters in close proximity to the pole, which produces the coldest observed locations on the lunar surface, including those where CO_2 ice ($\sim 54 \text{ K}$; Schorghofer et al. 2021) and H_2S ice ($\sim 51 \text{ K}$) are predicted to be stable at the surface. One potential challenge to accessing the wide diversity of volatiles predicted in these features is the high-relief topography and vast perennial darkness that define these larger permanently shadowed regions.

One of the quintessential PSR areas on the Moon is the cluster of craters near the south pole, including Haworth, Shoemaker, and Faustini craters, with Nobile also nearby (Figure 6(b)). Their preservation state and location provide a combination of conditions that can produce low surface temperatures. In addition to the three volatiles of interest tracked at Rozhdestvenskiy W, these craters contain regions where CO_2 ($\sim 54 \text{ K}$) and H_2S ($\sim 51 \text{ K}$) could be stable over long timescales, given sufficient supply to the region (Figures 4, 6). The potential variety of volatiles makes Haworth, Shoemaker, and Faustini advantageous for investigating the sum total of volatiles remaining in PSRs and characterizing the full extent of volatile species preserved on the Moon. However, the geological environment does not provide a flat surface traverse to a thermal safe haven area. Therefore, engineering a platform for long-term survival in the low-light, low-temperature environment would be challenging relative to Rozhdestvenskiy W and nearby Amundsen crater.

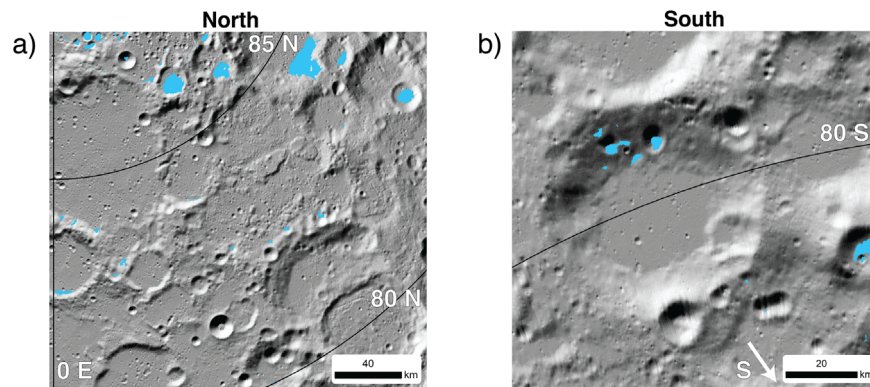


Figure 7. (a) Region of the north polar nearside that includes Nansen A ($\sim 82^\circ$ N, 64° E) and De Sitter M ($\sim 81^\circ$ N, 67° E) craters, where water ice deposits can be seen between 80° and 85° N. (b) Small impact craters on the rim of Newton A provide locations for $\lesssim 107$ K bolometric temperature measurements from Diviner.

Amundsen is a flat-floored complex crater, centered at $\sim 84^\circ$ S, 85° E and ~ 100 km in diameter. The shadow cast by the poleward-facing wall generates a region where sulfur (S_1), water, and hydrogen cyanide ices would all be thermally stable (Figure 6(c)). These regions appear on the floor of the crater close to the edge of the shadow, which would provide access to a mobile platform landed on the surface. The relative abundances of these volatiles would be proxies for the contribution to any extant deposits of the three different hypothesized sources of lunar polar volatiles. All of these volatiles have predicted thermal stability areas present in a relatively accessible location on the Amundsen floor. The small crater density is lower on the Amundsen crater floor versus the Rozhdestvenskiy W but would still offer the opportunity to observe a variety of thermal environments from a mobile or stationary platform. While supervolatiles like CO_2 and H_2S are not predicted to be stable at the surface on the Diviner scale, Amundsen hosts tracer volatiles of the three hypothesized mechanisms of volatile delivery to the Moon and is relatively accessible for a landed or mobile platform.

3.2. Nearside Off-polar Water Ice Patches

In addition to characterizing the thermal environments and thermal stability regions of volatiles in the relatively well-known, near-polar regions described above, we also found examples of lower-latitude, nearside surface water ice stability locations (Figure 7). Compared to the extreme poles, these locations would represent areas that could be visited for in situ sampling, avoiding the much larger cold, low-light conditions of the PSRs at Haworth, Shoemaker, and Faustini and would nonetheless provide similar insights into the nature and extent of water on the Moon. More explicitly, if water ice is present in surface thermal stability regions in areas adjacent to otherwise well-illuminated terrain, this would offer a constraint on the total amount of water ice and other volatiles delivered to the Moon and, depending on a small ice-rich feature's age, would constrain the timing of when the influx of water ice could have occurred.

In the north polar region, there are lunar nearside water ice patches between 80° and 85° N (Figure 7(a)). These include a crater on the rim of Nansen A ($\sim 82^\circ$ N, 64° E) where most of the floor has a temperature < 107 K. The outer rim of De Sitter M ($\sim 81^\circ$ N, 67° E) also contains roughness elements large enough to produce predicted water ice thermal stability locations on the Diviner scale. The north pole is also notable in that while many large, near-polar craters are lacking

compared to the south polar region, there are many water ice thermal stability regions associated with craters and post-impact modification of the crater's floor and rim. If surface water ice stability regions are a path to capture and bury water ice below the surface, then the spread of smaller water ice thermal stability regions at the north pole could be reflected in regional asymmetries in buried hydrogen content (e.g., Rubanenko et al. 2019).

Meanwhile, at the south pole there are some nearside water ice thermal stability regions that are more equatorward than 80° S. One example is a series of smaller craters that dot the southern rim of crater Newton A, a crater centered at $\sim 80^\circ$ S, 4° E with a diameter of ~ 300 km (Figure 7(b)). While Newton A itself is degraded enough to have a relatively flat floor, part of the degradation process at this crater has been new, smaller and deeper craters forming on top of it. The combination of smaller topographic elements on an already poleward-facing slope means that this water ice thermal stability region is dictated more by multiple shadowing from topography on orders-of-magnitude different spatial scales (e.g., Newton A is ~ 300 km in diameter, while the predicted water ice thermal stability region is due to a low area within one of the craters on the southern rim that is $\sim 2\text{--}3$ km long). As smaller craters are generated more frequently (e.g., Shoemaker et al. 1969), these superimposed craters on the Newton A rim are likely from a distinctly later time period than the formation of Newton A. Lower-latitude water-ice predicted thermal stability areas may be generally younger owing to their reliance on roughness generated by smaller geologic features like small impacts and mass wasting from crater rims. This means that there could be a way to piece together the history of lunar polar volatile delivery to the Moon by comparing some lower-latitude, smaller craters with predicted water ice thermal stability compared to the larger PSRs at Haworth, Shoemaker, and Faustini.

3.3. Area versus Latitude and Differences in Northern and Southern Hemispheres

The local geology at the north and south poles has similar local variations that provide environments with the potential to host a range of volatiles from different potential sources (volcanism, solar wind, asteroid/cometary impacts) and for water ice thermal stability equatorward of 85° latitude. Water is of great interest to addressing both scientific and exploration goals, and its thermal stability spans a broad range of latitudes at both poles. Total surface thermal stability areas for water ice and the other volatiles of interest are given in Table 1. Our

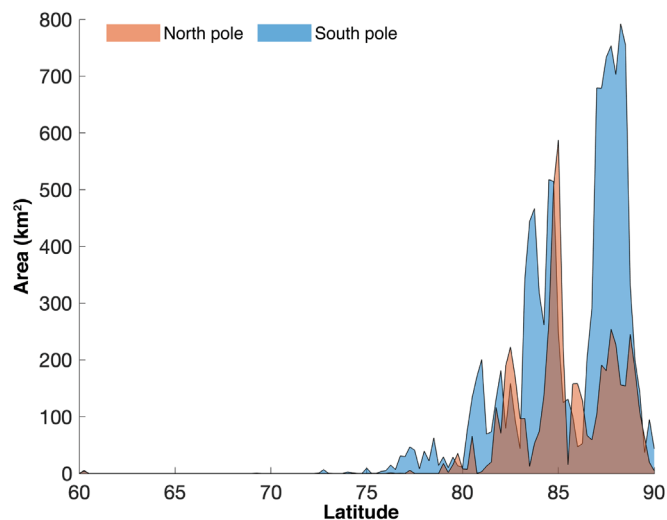


Figure 8. Area in square kilometers of water ice thermal stability in 0.25° latitude bins for the north (red) and south (blue) poles of the Moon based on the Diviner data presented here. The total areas and net distribution of the surface water ice thermal stability are different between the poles.

values for water ice surface thermal stability are systematically lower than those reported in Williams et al. (2019) because we use a temperature cutoff of 106.6 K instead of 110 K. When we recalculate our areas using 110 K as the temperature cutoff, our 80°–90° S area (1.337×10^4 km²) agrees to within 3% with the 1.30×10^4 km² given in Williams et al. (2019) for the same latitude range. This value is similar to the one reported from model predictions of surface thermal stability from Paige et al. (2010b) also for 80°–90° S, showing good agreement with initial models and data-driven thermal stability areas assuming the 110 K temperature for water ice thermal stability.

Generally, there are no significant regions $\lesssim 107$ K below $\sim 72^\circ$ latitude at either pole (Figure 8). Some small points are included in the bin that includes 60° S latitude, though this could be an artifact of the polar orbits of LRO achieving less spatial/temporal coverage at the lowest latitude examined in this data set and allowing for anomalously low temperatures. This effect is discussed in Williams et al. (2019), where effects from LRO’s orbit cause some areas, especially more equatorward, to not have the same spatial coverage as other locations closer to the poles. Due to LRO’s orbit, this effect is more pronounced in the south pole owing to the slightly smaller Diviner footprint size in the southern rather than northern hemisphere (Williams et al. 2019). Here we plot all areas based on the Diviner data, not just those regions detected in the map shape-file generation stage (see Section 2.3), and therefore multiple single-pixel cold locations are likely generating this increase in area. These 60° S pixels could also be reflecting cold areas within permanently shadowed regions identified by McGovern et al. (2013), who covered up to 65° S. The reconciling of 60° S cold pixels with ray-tracing from topography and data availability considerations is left to future work. While there are interesting outliers between 75° and 80° in both hemispheres, as well as the possibility of even more equatorward cold areas in the southern hemisphere, most of the water ice surface thermal stability area occurs poleward of 80° latitude.

There are two key differences in the north and south polar surface water ice thermal stability regions: the overall area and the latitudinal distribution of that area (Figure 8). Generally, the

water ice thermal stability area in the north polar region is about half that in the south pole (5513 km² from 60 to 90° N vs. 11,888 km² from 60 to 90° S), shown by the overall smaller area in Figure 8. The other key difference is that most areas within individual regions in the north pole are near $\sim 85^\circ$ N, while there is a much broader maximum peak near the south pole in area, from $\sim 85^\circ$ to 90° S. This means that most of the area $\lesssim 107$ K in the south polar region is also very near the pole, an area that is even colder owing to latitudinal effects. Both at the north pole and at south pole there are significant variations from a purely longitudinal trend, which would monotonically increase the thermal stability area for water ice with latitude if all other surface roughness elements were equal. This reinforces the importance of local topography and geologic chance (e.g., multi-km-diameter craters occurring closer to the pole than the equator in each hemisphere plus any effects of South Pole Aitken Basin) in understanding the thermal stability and evolution of lunar polar volatiles over lunar history. The hemispheric patterns in Diviner-predicted water-ice thermal stability matches previously reported evidence for greater infill of south polar lunar craters compared to the north, likely from water ice (e.g., Rubanenko et al. 2019), and further supports a potential link between understanding current surface water ice thermal stability and understanding how buried water ice on the Moon develops and remains stable.

3.4. Implications for Future In Situ Exploration

Depending on how lunar water is delivered to the surface and subsurface, there could be significant contamination of surface water ice deposits by other volatiles. Sulfur (S₁), which would be a major co-occurring volatile if lunar water was derived primarily from volcanism (e.g., Needham & Kring 2017), is stable within all of the same locations as surface water ice (Figures 2–5). If the volatile deposits from a volcanically derived lunar exosphere remained, we would expect traces of sulfur co-occurring with all surface water ice. In terms of the lunar surface sulfur species, our work indicates that corrosive hydrogen sulfide (H₂S I, stability temperature for ≤ 1 mm Gyr⁻¹ of ~ 51 K) is unlikely to be present in extensive deposits at the surface outside of a few square kilometers at the south pole. While it could be present in subpixel fractions elsewhere, it is less likely that these volatiles could survive in significant deposits at the lunar poles unless there was either a large or continuous supply, or if topographic and geologic conditions could result in rapid burial of the material during the era of significant lunar volcanism. The chemical evolution of these volatiles could also occur with time, which we largely leave to future work except to note that variations from predicted species volatile thermal stability could indicate this modification may have occurred either in a protolunar exosphere (e.g., Needham & Kring 2017) or after emplacement in the polar regions.

Volatiles that have known human health effects in sufficient doses, like mercury (Reed 1999) and toluene (delivered by comets; e.g., Bockelée-Morvan 2011), could occur in surface water ice deposits if they were supplied in sufficient quantities. Our maps indicate that toluene would co-occur with water ice in several locations (Figures 2–5), as both have similar stability temperatures (~ 88 K for toluene, ~ 107 K for water) higher than maximum annual polar temperatures (< 60 K) in spatially extensive cold traps, if toluene was ever significantly delivered. While toluene has been detected in comets (e.g.,

Schuhmann et al. 2019), it may be a small enough constituent to not form large deposits on the Moon. Hydrogen cyanide (stability temperature ~ 81 K) outnumbers toluene in comets and, while it is more volatile than toluene, is equally as problematic for humans and would likely occur in similar PSR environments to toluene and other cometary volatiles of interest. Therefore, determining the presence and relative abundance of these more volatile species is key for both understanding water delivery to the Moon and future in situ resource utilization by crewed missions.

Future work following on landing site selection for future volatile-focused lunar surface activity (e.g., Lemelin et al. 2014, 2021) can be informed by these thermal stability models to identify areas of highest priority for a variety of volatiles while also balancing needs of the spacecraft thermal systems or human health safety. High-priority locations from our analysis alone would include Amundsen crater and other locations where tracer volatiles of potential lunar outgassing, cometary delivery, and solar wind would be thermally stable together, e.g., Figure 6. Landing site selection for future missions takes into account many factors, and our maps of predicted thermal stability for a variety of volatiles are one additional data set available to further refine those selections.

4. Conclusions

Based on Diviner lunar radiometer data, we identify regions where volatiles of interest would be stable on the lunar polar surface over billion year timescales given the current lunar surface temperatures from 60° to 90° latitudes in both hemispheres, if they had ever been delivered to the Moon. From this, we identify several locations at the north and south pole where it is possible for tracer volatiles from lunar volcanism, solar wind, and small body impact delivery to be stable over geologic time (e.g., ≤ 1 mm Gyr^{-1}) and where they could be accessible for in situ exploration to determine the relative abundance and therefore likely sources. We also identify multiple low-latitude ($< 85^\circ$ and some below 80°) areas of surface water ice thermal stability on the lunar nearside that may provide locations where direct measurements of the presence of water ice could begin to unravel the temporal history of water delivery to the Moon. Finally, we show that the overall latitudinal trends in surface water ice thermal stability regions from Diviner data are strikingly different in the north and south poles in both total area and area distribution, which might shed light on the key role that topography plays in determining the distribution of surface volatiles on the Moon, especially from features like large craters that are stochastic in nature.

This work was made possible through support from NASA's Lunar Reconnaissance Orbiter project and Lunar Flashlight programs. Diviner data are available on the Planetary Data System (PDS) at <https://pds-geosciences.wustl.edu/missions/lro/diviner.htm>. Temperature maps and volatile maps for all volatiles of interest listed in Table 1 are included in supporting information available from the CU Scholar repository at doi:10.25810/gkdf-n764. Where a volatile map does not exist, the total effective stability area was less than 1 map pixel. The files are in GIS format and show the data from Figures 2–5. The repository also includes the maximum bolometric

temperature data (north and south poles), in CSV format. This is the data behind Figure 1.

Orbits 243, 274, 283, 288 3992, 3979, 4018, 7725, 8190, 8625, 11448, 13411, 13419, 15717, 17740, 20667, 29206, 30909, 37317, 37270, and 37292 were manually omitted from the Diviner data set.

A. Springmann assisted with paper typesetting and presentation in L^AT_EX.

We acknowledge our peers in biological science research, as well as health care and other essential workers, whose hard work and sacrifice have allowed us to conduct a portion of this research during the COVID-19 pandemic.

ORCID iDs

Margaret E. Landis  <https://orcid.org/0000-0001-7321-2272>

Paul O. Hayne  <https://orcid.org/0000-0003-4399-0449>

Jean-Pierre Williams  <https://orcid.org/0000-0003-4163-2760>

4163-2760

Benjamin T. Greenhagen  <https://orcid.org/0000-0002-8252-9922>

8252-9922

References

- Bandfield, J. L., Hayne, P. O., Williams, J.-P., Greenhagen, B. T., & Paige, D. A. 2015, *Icar*, **248**, 357
- Bockelée-Morvan, D. 2011, IAU Symp. 280, The Molecular Universe (Cambridge: Cambridge Univ. Press), 261
- Clarke, S. W. 2019, Explore Science: Science Exploration Update in 46th Space Congress, <https://commons.erau.edu/space-congress-proceedings/proceedings-2019-46th/presentations/38/>
- Colaprete, A., Schultz, P., Heldmann, J., et al. 2010, *Sci*, **330**, 463
- Davidsson, B. J. R., & Hosseini, S. 2021, *MNRAS*, **506**, 3421
- Feldman, W. C., Maurice, S., Binder, A. B., et al. 1998, *Sci*, **281**, 1496
- Gibson, E. K., & Moore, G. W. 1973, *Sci*, **179**, 69
- Hayne, P. O., Aharonson, O., & Schörghofer, N. 2021, *NatAs*, **5**, 169
- Hayne, P. O., Greenhagen, B. T., Foote, M. C., et al. 2010, *Sci*, **330**, 477
- Hayne, P. O., Hendrix, A., Sefton-Nash, E., et al. 2015, *Icar*, **255**, 58
- Killen, R. M. 2003, *M&PS*, **38**, 383
- Lemelin, M., Blair, D. M., Roberts, C. E., et al. 2014, *P&SS*, **101**, 149
- Lemelin, M., Li, S., Mazarico, E., et al. 2021, *PSJ*, **2**, 103
- Li, S., Lucey, P. G., Milliken, R. E., et al. 2018, *PNAS*, **115**, 8907
- Mazarico, E., Neumann, G. A., Smith, D. E., Zuber, M. T., & Torrence, M. H. 2011, *Icar*, **211**, 1066
- McCord, T. B., Taylor, L. A., Combe, J. P., et al. 2011, *JGRE*, **116**, E00G05
- McGovern, J. A., Bussey, D. B., Greenhagen, B. T., et al. 2013, *Icar*, **223**, 566
- Meyer, B. 1964, *ChRv*, **64**, 429
- Morgan, T. H., & Shemansky, D. E. 1991, *JGR*, **96**, 1351
- Needham, D. H., & Kring, D. A. 2017, *E&PSL*, **478**, 175
- Paige, D. A., Foote, M. C., Greenhagen, B. T., et al. 2010a, *SSRv*, **150**, 125
- Paige, D. A., Siegler, M. A., Zhang, J. A., et al. 2010b, *Sci*, **330**, 479
- Pieters, C. M., Goswami, J., Clark, R., et al. 2009, *Sci*, **326**, 568
- Reed, G. W., Jr. 1999, *M&PS*, **34**, 809
- Rubanenko, L., & Aharonson, O. 2017, *Icar*, **296**, 99
- Rubanenko, L., Venkatraman, J., & Paige, D. A. 2019, *NatGe*, **12**, 597
- Schörghofer, N., Williams, J., Martínez-Camacho, J., Paige, D. A., & Siegler, M. A. 2021, *GeoRL*, **48**, e95533
- Schörghofer, N., & Williams, J.-P. 2020, *PSJ*, **1**, 54
- Schuhmann, M., Altwegg, K., Balsiger, H., et al. 2019, *A&A*, **630**, A31
- Schultz, P. H., Hermalyn, B., Colaprete, A., et al. 2010, *Sci*, **330**, 468
- Sefton-Nash, E., Williams, J. P., Greenhagen, B. T., et al. 2019, *Icar*, **332**, 1
- Shearer, C. K., Hess, P. C., Wieczorek, M. A., et al. 2006, *RvMG*, **60**, 365
- Shoemaker, E. M., Batson, R. M., Holt, H. E., et al. 1969, *JGR*, **74**, 6081
- Siegler, M. A., Miller, R. S., Keane, J. T., et al. 2016, *Natur*, **531**, 480
- Stüdel, R., & Eckert, B. 2003, Elemental Sulfur and Sulfur-Rich Compounds I. Topics in Current Chemistry, Vol. 230 (Berlin: Springer), 1
- Williams, J.-P., Greenhagen, B. T., Paige, D. A., et al. 2019, *JGRE*, **124**, 2505
- Williams, J.-P., Paige, D., Greenhagen, B., & Sefton-Nash, E. 2017, *Icar*, **283**, 300
- Zhang, J. A., & Paige, D. A. 2009, *GeoRL*, **36**, L16203